

In-orbit performance of the XMM-Newton X-ray telescopes: images and spectra

B. Aschenbach

Max-Planck-Institut für extraterrestrische Physik,
Postfach 1312, 85741 Garching, Germany

ABSTRACT

The XMM-Newton X-ray Observatory was launched by an ARIANE V from Kourou, French Guiana, on 10 December 1999. First light was received by one of the three X-ray telescopes on 19 January 2000. Since then an extensive program, comprising commissioning, calibration and performance verification of the scientific payload, has been carried out, followed by regular scientific Guaranteed Time Observations which are interleaved with observations drawn from the Guest Observer (AO-1) program. I present the in-orbit performance of the three X-ray telescopes and demonstrate the excellent agreement with the ground calibration measurements. This includes the imaging characteristics both on-axis and off-axis, the effective collecting area and vignetting making use of in-orbit images and spectra. The scientific impact of a few of these observations is highlighted as well.

Keywords: XMM-Newton, X-ray telescopes, X-ray optics testing, X-ray straylight

1. INTRODUCTION

On December 10 1999 the XMM spacecraft was placed in a 48h Earth orbit by the first commercial ARIANE V launcher. XMM, or X-ray Multi-Mirror Mission, re-named XMM-Newton after its successful launch, is the second cornerstone of the Horizon 2000 science program of the European Space Agency ESA. XMM-Newton was designed as a facility class X-ray astronomy observatory to study cosmic X-ray sources spectroscopically with the highest collecting area feasible in the 0.1 - 10 keV band. Over the full band moderate spectral resolving power between 1 and 60 is required and medium resolving power of ≥ 250 was aimed for in the 0.1 - 3 keV band. The high throughput is primarily achieved by a set of 3 imaging, highly nested Wolter type I telescopes. The imaging performance of each of the grazing incidence mirror systems was originally set to be better than 30 arcsec for the half energy width (HEW) of the point spread function (PSF) with a goal of 10 arcsec. In a first attempt the scientific requirements have been put together at a workshop held at Lyngby, Denmark, in June 1985¹. A detailed analysis of the types of telescopes with which these requirements could be achieved was carried out by the ESA established Telescope Working Group, which also arrived at a first telescope design^{2,3,4}. Over ten years in time the design was put into reality, the telescopes were built in industry including Carl Zeiss, Oberkochen in Germany, Kayser-Threde, Munich in Germany and Media Lario, Bosisio Parini in Italy. The development and building of the mirror shells up to the flight mirror modules was accompanied by X-ray tests in the 130 m long X-ray test facility PANTER of the Max-Planck-Institut für extraterrestrische Physik. The qualification of the mirror modules was performed in EUV light at the Focal-X facility of the Centre Spatial de Liège in Belgium. A more detailed overview of the mission, the spacecraft and mission operations can be found in reference 5. Some analysis and summary of the ground calibration of the X-ray telescopes prior to launch is provided by Gondoin et al.^{6,7}.

One of the X-ray telescopes is equipped with a focal plane imaging camera of pn semiconductor CCD technology^{8,9} (EPIC-pn) and each of the other two telescopes has a MOS CCD X-ray camera in the focal plane¹⁰ (EPIC-MOS1 and EPIC-MOS2). Each of these two cameras receive $\sim 50\%$ of the X-ray light leaving the exit plane of the corresponding X-ray telescope whereas the other half of the X-ray beam is intercepted by an array of grazing incidence gratings, part of the reflection grating spectrometers^{11,12} (RGS1 and RGS2). The X-ray payload is complemented by the optical/UV monitor telescope OM¹³.

B.A.: Email: bra@mpe.mpg.de

First light was received by the X-ray telescope equipped with the EPIC-pn camera on 19 January 2000 when it was pointed towards the 30 Doradus region in the Large Magellanic Cloud^{14,15} with the other instruments following within days. The initial phase of operations and scientific observations was devoted to commissioning and calibration of the system, subsystems and the scientific instruments. Thereafter an extended period of performance verification followed until July 2000. Some of the scientific results of this first half year of XMM-Newton observations were published in a special issue of *Astronomy & Astrophysics*¹⁶. From July 2000 on observations of the Guaranteed Time Observing Program interleaved with observations of the first Guest Observer Program (AO-1) were carried out. Until early July 2001 data sets of ~ 400 observations have been delivered to the original proposers.

The present paper focuses on the in-orbit performance of the three X-ray telescopes. The derivation of the performance parameters like point spread function (PSF), effective collecting area and vignetting of just the telescopes is not an easy task, since the measurements always involve the focal plane instruments and/or the reflection grating assembly which have their specific performance, so that the determination of the mirror PSF is intimately linked to the pixel size, photon pile-up, pattern pile-up, read-out mode, photon and charged-particle background, etc. of the CCD detectors. Likewise is the effective area determination sensitive to the CCD quantum efficiency, charge-transfer inefficiency and read-out mode of the CCDs, etc. Since the wings of the mirror PSF spread out over several independent and individual CCDs, which have different characteristics, in particular different background levels, the PSF is not easily established from a few imaging observations, likewise is the vignetting. Calibration work is still in progress, but the core of the PSF is understood and the collecting area is being close to be understood. At low energies, i.e. < 1 keV, the energy dependent transmission of the various absorption filters used in front of the CCDs complicates the issue of calibration of the effective collecting area, which is not settled, yet.

Independent of the still standing issues of calibration the observations which are at hand clearly demonstrate that the scientific instruments on XMM-Newton are fulfilling their scientific capabilities qualitatively and quantitatively to the level the design promised many years ago.

After a short description of the telescopes' design and its criteria followed by an outline of the manufacturing process of the mirrors the in-orbit imaging performance of the three X-ray telescopes is presented and confronted with the full X-ray beam calibration measurements taken at the PANTER. The second half of the paper is used to illustrate the scientific capabilities of XMM-Newton summarizing a few observations and the scientific progress made by them.

2. THE X-RAY TELESCOPES

2.1. Design

The design of the optics was driven by the requirement of obtaining the highest possible effective collecting area over a wide band of energies up to 10 keV and more with particular emphasis on the region around 7 keV, in which the K lines of the astrophysically important iron appear. Thus, the mirror system has to utilize a very shallow grazing angle of $\sim 0.5^\circ$ in order to provide sufficient reflectivity at high energies. In grazing incidence optics the effective area is increased by nesting a number of mirrors and thus filling the front aperture as far as possible. The nesting efficiency is determined by the mirror shell thickness and, in case of very low grazing angles for high energy optics, by the minimum radial mirror separation which is required for integration and alignment. The thinner the mirror shells are and the narrower the shells are spaced the larger is the collecting area. In the past very thin aluminum foils shaped to double cones have been used. Thin-walled mirrors have also been produced by replication techniques and electroforming. Electroformed mirrors have been built up mostly in solid nickel, which, however, suffer from high mass. For the design calculations the shell thickness was assumed to increase approximately linear with shell diameter to guarantee sufficient stiffness. A minimum radial shell separation of 1 mm was considered to be feasible to handle the integration of the shells in a package. Both the paraboloid section and the hyperboloid section were replicated as a single piece from a single mandrel, which limited the axial length of the total mirror to 60 cm. The length is shared evenly by the paraboloid and the hyperboloid. Although longer mirrors would have provided a larger collecting area they were discarded because they were suspected to be very difficult to be removed from the mandrel. The production of paraboloid

and hyperboloid in one piece avoids the problems created by the additional tasks of aligning and mounting if paraboloid and hyperboloid are separate. Given the length constraints imposed by the launcher the focal length was fixed at 7.5 m. The optimum design, which fulfills the collecting area constraints, was found by ray tracing. Gold was considered as baseline for the mirror surface coating; attempts to produce replicated mirrors with an iridium coating, which would have provided somewhat better high energy response, failed because the adhesive forces of iridium on the mandrel surface turned out to be too strong so that patches of the iridium layer tended to stick on the mandrel. Eventually the mirror wall thickness was fixed to 1 mm for the outermost shell with a diameter of 700 mm and at 0.5 mm for the innermost shell of 306 mm diameter. Each mirror assembly contains 58 shells; adding more shells is rather inefficient in building up more collecting area because of the mass penalty involved and the low gain in effective area.

2.2. Manufacturing

The production of nickel shells involves three steps. As for any replication a master mandrel of negative shape is produced for each of the 58 mirror shells. The mandrel is of solid aluminum covered with a thin layer of Kanigen, which is ground and polished to the precise negative shape of the required mirror. The mandrel surface is measured by metrology means, including profilometers of various trace lengths and interferometers. Ray tracing of the metrology data reveals that the XMM mandrels have an angular resolution of ≤ 5 arcsec HEW and an rms surface microroughness of ≤ 0.5 nm. The mandrels are coated with a gold layer ~ 200 nm thick. Each mandrel is put in an electrolytical bath in which a nickel layer is being built upon the gold surface until the required thickness has been reached. By cooling the nickel shell separates from the mandrel, whereby the gold surface sticks to the electroproduced nickel shell because of the higher adhesion forces. After separation the nickel shells are exclusively supported by 16 strings threaded through 16 tiny holes which are equally spaced around the circumference of the mirror closely below the rim of the paraboloid. After inspection of the surface and measurement of a couple of meridional profiles each mirror is mounted to a spider like support structure by glueing the parabola mirror into small grooves in each of the 16 arms of the spider. This is done with the mirror oriented vertically and under optical control. The spider support structure at the paraboloid front is the only support structure of the mirror shells. There is no counterpart at the aft of the hyperboloids; they are not constrained or supported mechanically at all. A close view of one mirror module sector out of the 16 sectors is shown in Figure 1a. Further details about the production of the XMM telescopes are given by de Chambure et al.¹⁷.

2.3. The X-ray Baffle

From an X-ray optical point of view a telescope is to be complemented by an X-ray baffle, which eliminates X-ray straylight from sources outside the field of view. Rays from outside the field of view can reach the sensitive area of the focal plane detectors by single reflection from the rear end of the hyperbola, if the source is at an off-axis angle between 20 arcmin and 80 arcmin, in case of XMM-Newton. Rays reflected just once from any one of the parabolas cannot leave the mirror assembly because of the close packing of the mirror shells. Less highly nested telescopes like those on the Einstein, ROSAT and Chandra observatories employ radial vanes with one set inside and one set in front of each mirror to eliminate singly reflected rays. A set of vanes inside of the XMM-Newton mirror modules was excluded because of the high mechanical complexity involved, but it was found that an external multi-stage baffle could completely eliminate singly reflected rays. The concept foresees a set of concentric cylinders¹⁸, one for each mirror shell, placed in front of the mirror system. Each ring has an annular width slightly thinner than the corresponding mirror wall thickness and a cylindrical height characteristic for each mirror by which the singly reflected rays are blocked. Because of the mechanical complexity together with the limited space available the design was simplified to two parallel annular plane sieve plates of equal thickness. Each plate consists of 58 rings and 16 radial struts. The plates are mounted co-axial to and co-aligned with the front aperture cross section of the 58 mirror shells. The off-set of the two sieve plates from the front of the mirror system is 385 mm and 439 mm, respectively¹⁹. The efficiency of the sieve plate system has been ray traced and demonstrated to reduce the straylight level by a factor of 5 to 10 depending on the position in the focal plane. Figure 1b shows the image of a region of the Large Magellanic Cloud which is centered close to the pulsar PSR 0540-69.3 and an associated supernova remnant. In the lower right the typical pattern of singly reflected rays

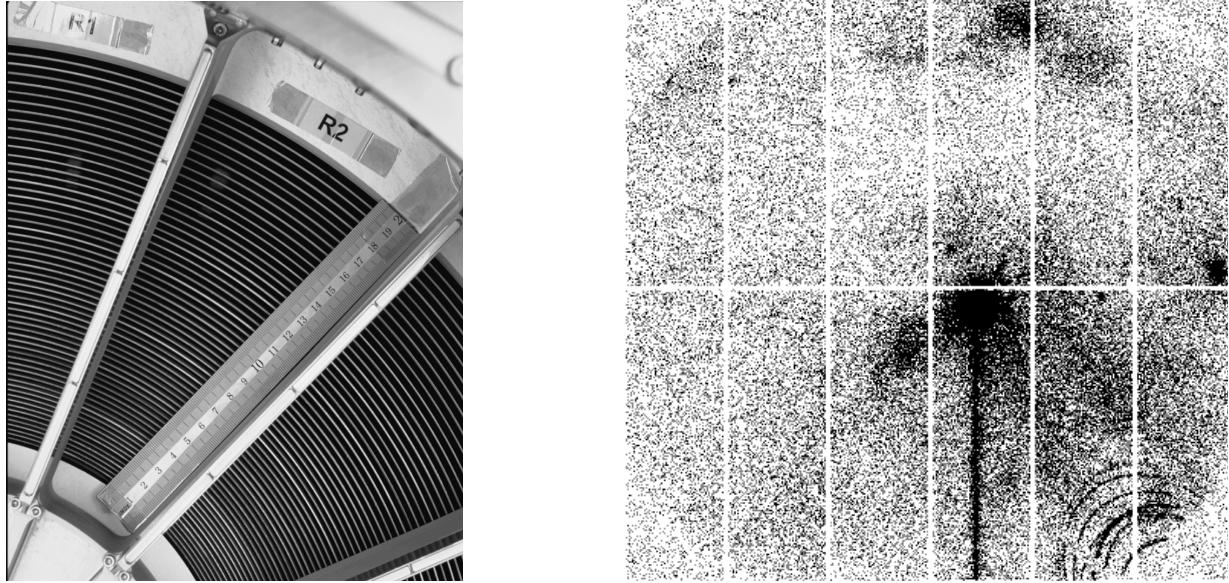


Figure 1. Fig. 1a (*left*): Rear view of one sector of the XMM-Newton mirror assembly FM2 showing the 58 shells. The struts are elements of the electron deflector. Fig. 1b (*right*): X-ray image of the supernova remnant and pulsar PSR 0540-69.3 (close to image center) taken with the EPIC-pn camera. In the lower right corner sections of rings appear which are due to singly reflected rays from a point source outside the field of view to the lower right.

from a bright point source outside the field of view can be seen. The level of stray light flux received in the image confirms the efficiency of the X-ray baffle expected from ray-tracing calculations for the nominal configuration.

A complete overview of the telescope with all its subsystems including the mirror door, the entrance optical baffle, the electron deflector and additional support structure is given in Ref. 17.

2.4. X-ray calibration on ground

During Phase C/D of the XMM program five X-ray mirror modules have been built three of which have been selected for flight, i.e. FM2, FM3 and FM4. FM1 and FM5 have been kept as spares, numbering of the modules is in chronological order of production. X-ray testing and final X-ray calibration including measurement of the PSF both on-axis and off-axis for a few energies between 0.28 keV and 8.05 keV and the effective area as well as the vignetting function for a series of energies covering the range from 0.28 up to 17 keV has been performed in MPE's PANTER test facility between April 1997 (FM1) and July 1998 (FM4). MPE's PANTER originally built for the development and calibration of the ROSAT X-ray telescope was modified and partially rebuilt in 1992/93 to cope with the size of the XMM telescopes and quality assurance requirements. In simple terms, the facility consists of a 130 m long vacuum pipe of 1 m diameter. At the one end a micro-focus characteristic X-ray line source is installed and the use of various anti-cathode materials provides the required coverage of the energy band. The X-ray source has a diameter of ~ 1 mm. At the other end a huge cylindrical vacuum tank 12 m long and 3.5 m in diameter houses the X-ray telescope to be tested. The typical distance between source and mirror module midplane, i.e. the paraboloid hyperboloid intersection, is ~ 124 m. With a focal length of 7.5 m the image of the X-ray source is produced at a distance of 7.97 m measured from the mirror module midplane. Given these distances the angular size of the X-ray source is ~ 1 arcsec, which means that structures of the mirror surface finer than this cannot be resolved.

Both full aperture measurements and sub-aperture measurements have been performed. The PSFs and the effective collecting area were measured with the entire aperture of the mirror module illuminated, implying a beam divergence between 8.5 arcmin and 19.5 arcmin full width between the innermost and outermost mirror shells. The divergence of the illuminating beam implies that the rays reflected off the frontal one third of the parabolas do not intersect with the hyperboloids. Therefore the surface of this section of the parabolas is not

imaged and does not contribute to the PSF. Furthermore the corresponding reflection loci on parabola and hyperbola differ from those for on-axis parallel beam illumination. Images have been recorded with both a position sensitive proportional counter (PSPC) which is a copy of the PSPCs flown on-board of ROSAT²⁰ and an X-ray CCD provided by the X-ray astronomy group of the University of Leicester in the UK. Whereas the PSPC is well suited to measure effective area and the wings of the telescope PSF the CCD with its significantly better spatial resolution has been used to assess the details of the PSF core out to angular distances of ~ 125 arcsec limited by the linear size of the CCD. The PSPC has a larger field of view and the PSF can be traced out to angular distances of 984 arcsec. The comparison of the CCD and the PSPC encircled energy functions show that the CCD images out to 125 arcsec contain 97% of the total flux at 1.5 keV and 93% at 8.05 keV, respectively.

Measurements of the effective collecting area were also done using smaller apertures to reduce the beam divergence. The open area of such an aperture is defined by the azimuthal width of one sector of the mirror module, i.e. 22.5° , and the radial width corresponds to roughly one quarter of the radial extent of the mirror assembly defined by the radii of the outermost and innermost shells. In this way the full aperture is sampled by 64 sub-apertures. The sub-apertures were realized by two steel plates with appropriate cut-outs, which were placed roughly 0.5 m in front of the mirror module. By rotating the two plates against each other like a fortune wheel or 'Glücksrad' any one of the 64 sub-apertures could be set up. The maximum beam divergence is <1.4 arcmin which is much closer to a parallel beam configuration than for the full aperture illumination.

2.5. Point spread function

On January 19 2000 the X-ray telescope FM2 saw "First Light" of the X-ray sky^{14,15} followed by FM3 and FM4 two days later. Two different X-ray cameras are used to record the X-ray images. In the focal plane of FM2 a novel type of X-ray CCD based on pn-technology is used (FM2/pn)^{8,9} whereas FM3 and FM4 each are equipped with a more conventional CCD based on MOS-technology¹⁰ (FM3/MOS1 and FM4/MOS2). Unlike FM2, FM3 and FM4 each carry a reflection grating spectrometer (RGS)^{11,12} by which about half of the X-ray beam is diverted from MOS1 and MOS2. After "First Light" the imaging performance of the three telescopes was of immediate interest and additional observations were made during the commissioning phase of XMM-Newton until March 8 2000. Sources studied include the sources of the "First Light Field" to the Large Magellanic Cloud and the point sources EXO 0748-67, LMC X-3, PSR 0540-69 and PKS 0558-504. To circumvent pile-up problems in the CCDs only observations taken in "small window" mode were used for the early assessment of the in-orbit PSF. In "small window" mode, however, the observational field is limited in size and the radial extent of the PSF which can be studied is limited accordingly. The PSFs taken on ground can therefore only be compared with the in-orbit results out to the angular distance imposed by the "small window" size, which is ~ 30 arcsec in radius. The wings of the PSFs are not accessible with these early measurements. Likewise, the encircled energy functions, i.e. the radially integrated PSFs, have been normalized to the value measured on ground at the angular distance corresponding to the "small window" size.

A major difference between the conditions on ground and in orbit is the type of detector used in the focal plane, in particular the pixel size. The CCD used on ground had a pixel size of $25 \mu\text{m}$ equivalent to 0.65 arcsec. The CCDs used in orbit have a pixel size of $40 \mu\text{m}$ for the MOSs and $150 \mu\text{m}$ for the pn, which relates to 1.1 arcsec and 4.1 arcsec, respectively. In particular the pn-CCD pixel size appears too large to resolve the core of the PSF directly and simulations still have to be done to demonstrate the compatibility with the ground measurements.

The results of this early analysis have already been reported²¹ and only the results for FM4 coupled to EPIC-MOS2 are repeated here in Figure 2. Ref. 21 summarizes the imaging performance of all three telescopes. The data show that the performance in orbit is basically the same as it was on ground for all three telescopes as far as the PSF out to ~ 30 arcsec is concerned. Work is in progress to extend the analysis to image radii >30 arcsec, which is hard because of the difficulty to assess the background in the cameras properly and because the individual CCDs in both the pn and MOSs cameras show different performance making the the relative adjustment among the CCDs tedious and cumbersome. However, given the excellent agreement of the PSFs between the ground and in-orbit measurements as far as the core of the PSF is concerned there is no major difference for the PSF wings between ground and in-orbit performance expected. I have therefore merged the

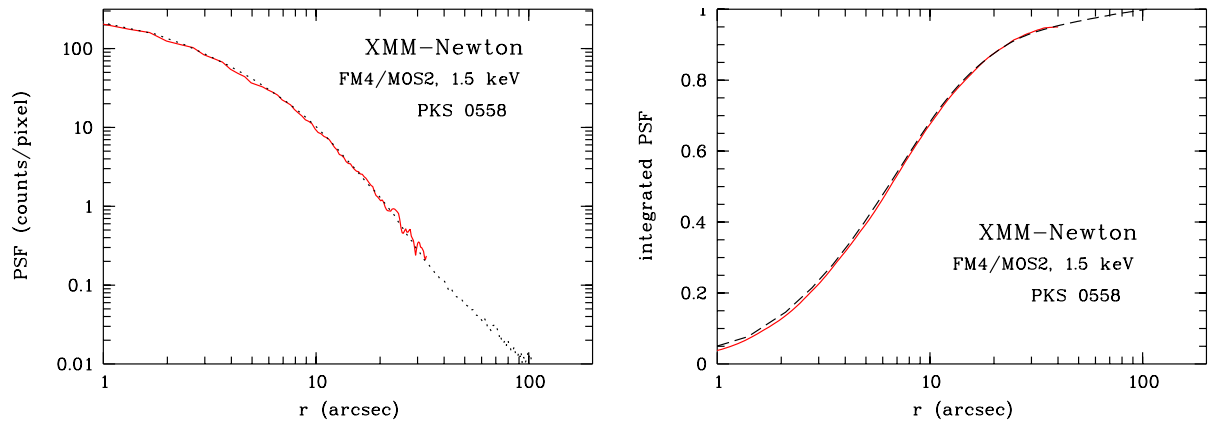


Figure 2. Point spread function (Fig. 2a, *left*) and encircled energy function (Fig. 2b, *right*) of mirror module FM4 (solid line: in orbit, dotted/dashed line: on ground).

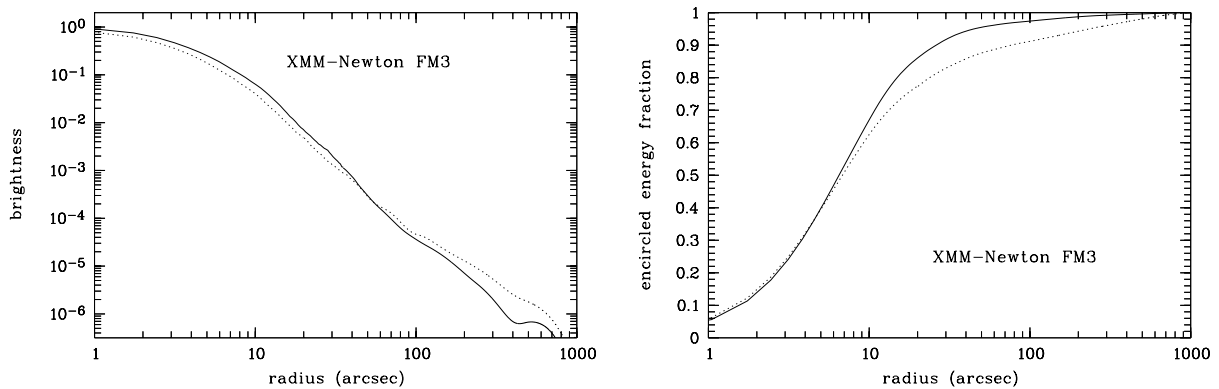


Figure 3. Point spread function PSF (Fig. 3a, *left*) and encircled energy function EEF (Fig. 3b, *right*) of mirror module FM3 measured at PANTER combining the CCD and PSPC measurements (solid line: 1.5 keV, dotted line: 8 keV). PSF and EEF are normalized to unity for the flux within 984 arcsec image radius, both for 1.5 and 8 keV.

PSF ground measurements at PANTER taken with the CCD and the PSPC to construct the joint PSF and associated encircled energy function (EEF) out to image radii of 984 arcsec. The results for FM3 are shown in Figure 3. I expect the PSF and the EEF in orbit very close to the results shown. Figure 3 illustrates the fairly weak dependence of the PSF and the EEF for energies between 1.5 keV and 8 keV. I don't expect this to be different for FM2 or FM4 given the ground measurements.

Figure 4a shows the 2-D PSF of FM3 for a point source in terms of iso-brightness contours. The contours illustrate the capability to resolve structures down to a few arcseconds. This capability is convincingly demonstrated by Figure 4b, which shows the X-ray image of the Castor A/B binary system together with YY Gem or Castor C, another binary taken with the EPIC-MOS1 camera. Castor A and B are known to be separated by 3.9 arcsec, and they are clearly resolved in the image. Even the flaring of either of the two stars and the associated temporal change of the X-ray flux can be monitored and attributed to one or the other star²².

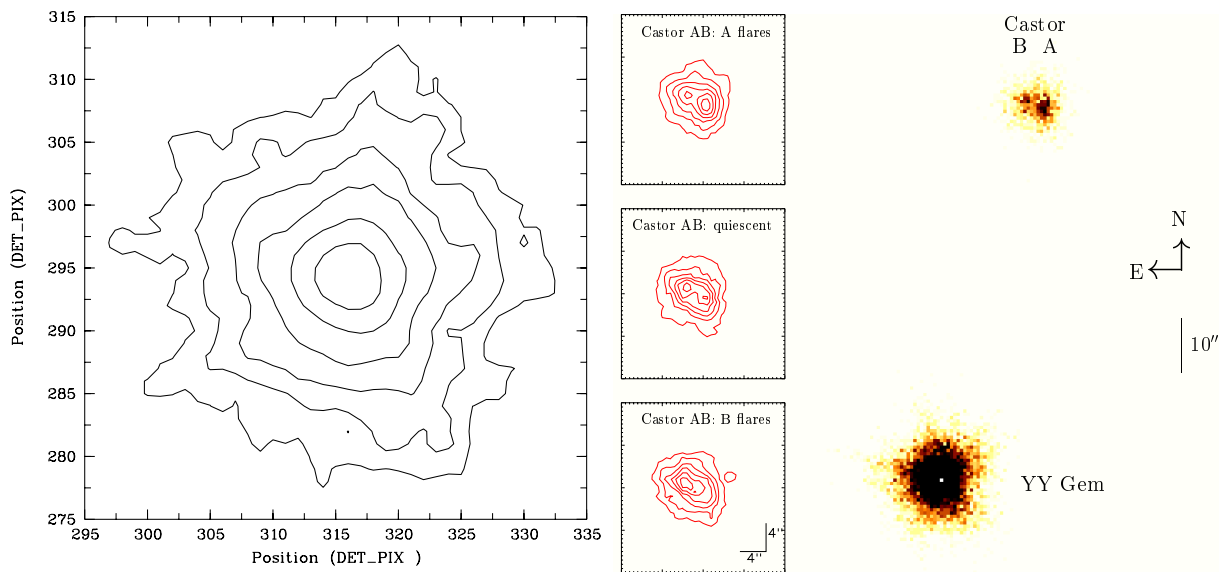


Figure 4. Fig. 4a (*left*): Surface brightness of a point source image taken with mirror module FM3 in orbit. The size of the frame is $44''$ by $44''$. Contours are stepped by a factor of two in brightness²¹. Fig. 4b (*right*): X-ray image of the Castor A/B and YY Gem system taken with the FM3 EPIC-MOS1 instrument; Castor A and B, which are separated by 3.9 arcsec are resolved.²²

2.6. Effective collecting area

The design driver for the XMM-Newton telescopes' geometry was to achieve maximal area at low energies (2 keV) without sacrificing area at high energies (~ 7 keV). The design promises a collecting area of the mirror assembly approaching 1900 cm^2 for energies up to 150 eV, $\sim 1500 \text{ cm}^2$ at 2 keV, 900 cm^2 at 7 keV and 350 cm^2 at 10 keV for each of the three telescopes on-axis. At 15 keV the area drops to $\sim 12 \text{ cm}^2$. The effective area for each of the telescopes was measured in MPE's PANTER X-ray test facility illuminating the full aperture with characteristic line radiation between 0.28 keV and 10 keV and using a copy of the ROSAT PSPC as focal plane detector. The diameter of the PSPC in conjunction with the XMM-Newton telescopes corresponds to a field of view of 984 arcsec radius, so that at higher X-ray energies some fraction of the effective area is likely to be missed because rays are scattered outside of the field of view due to mirror surface microroughness. The results are compared with predictions from ray-tracing calculations taking into account the nominal mirror shell geometry, the test facility geometry (beam divergence) and using the optical constants of gold originally published by Henke et al.²³. Up-to-date data, which have been used here, are found in ref. 24. Figure 5a shows that the maximally achievable area appears not to have been met, but instead a deficit of $\sim 15\%$ on average is apparent. At fixed energy the spread in area among the four telescopes is relatively low of 2 to 3% at most. The deficit has been analysed by Gondoin et al.⁷, drawing upon additional dedicated reflectivity measurements carried out at PANTER. The main contributors are identified as mirror edge deformations, causing additional obstruction in the PANTER divergent beam, and reflectivity losses. The sub-aperture tests at PANTER using the 'Glücksrad' configuration with the much better collimated beams confirmed the additional shadowing by the extended edges, as the effective area turned out to be higher. The deficit in area is reduced at all energies and the remaining deficit of $\sim 7\%$ on average is attributed to intrinsic reflectivity losses which amount to 3 to 4% relative per reflection (c.f. Figure 5b). At higher energies (>3 keV) the deficit becomes slightly larger than the average because of increasing mirror surface scattering. These measurements are the basis for the in-orbit calibration files for the XMM-Newton X-ray telescope effective area. Figure 6a illustrates the difference between a perfect mirror module of perfect reflectance and zero scattering and the in-orbit performance described by the current calibration file. The difference follows basically the 'Glücksrad' measurements except for the energies which are

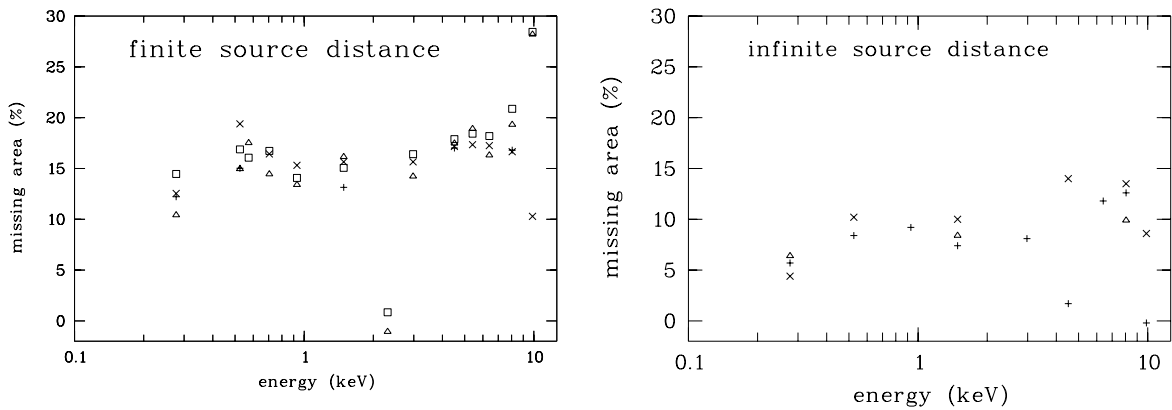


Figure 5. Fig. 5a (*left*): Apparent effective area deficit of the XMM-Newton mirror modules FM1 (triangle), FM2 (+), FM3 (x) and FM4 (square) measured at PANTER with the full aperture illuminated. Fig. 5b (*right*): Effective area deficit of the XMM-mirror modules FM1 (triangle), FM2 (+) and FM3 (x) deduced from 64 sub-aperture measurements using the 'Glücksrad' configuration, which provides a close to 'infinite source distance' configuration. Maximal area data assume perfect reflectance and nominal mirror module geometry.

close to the M-absorption and L-absorption edges of gold, at which the area recommended by the calibration file differs significantly from expectation. In particular the region of the M-edges around 2.3 keV is of concern. In-orbit spectra of negligible statistical errors and simple shape like power laws taken with the EPIC cameras show strong residuals when fitted which indicates a collecting area different from the calibration file. Further work is required, also to investigate whether the energy levels and the optical constants given in the literature are actually correct. Work by Owen et al.²⁵ indicates some difference.

The real test of the accuracy of the calibration data comes via the comparison and fits to the spectra of well-known sources keeping in mind that it is not only the mirror but eventually the entire instrument including the focal plane camera which is being tested. Willingale et al.²⁶ report a maximum difference between previous measurements of the Crab Nebula and the results obtained with the EPIC-MOSs of 5% as far as the normalization of the spectrum is concerned. The pure statistical error might be even less. This supports very much the current calibration of the telescopes for energies above ~ 0.8 keV, where the Crab spectrum is bright. A cross-calibration between the EPIC MOS cameras and the EPIC-pn camera in this energy band, i.e. for energies >1 keV, has been derived by Warwick et al.²⁷ who did a simultaneous fit of all three EPIC cameras to the spectra of the supernova remnant G21.5-0.9. Both the slope of the power law spectrum and the normalization agree within the statistical error, which is 2% and 5% respectively. It appears that the broad band calibration of the mirror modules' effective area is without problems; the clarification of details around the gold absorption edges and the calibration at low energies (<1 keV) are still pending.

The decrease of the effective area with increasing field angle is described by the vignetting function, which is the ratio of the off-axis area and on-axis area at fixed energy. The assessment of the vignetting function is important to describe the flux of off-axis point sources and extended sources like supernova remnants and clusters of galaxies. Since the EPIC field of view is covered by several independent CCDs both for the MOS cameras and the pn camera, any one of which has different properties, the vignetting function is difficult to be assessed quantitatively. Some attempts have been made by putting G21.5-0.9, a supernova remnant roughly 5 arcmin in diameter, at various field positions. The result in terms of the vignetting function at 10 arcmin is shown in Figure 6b for the MOS camera. The data are compared with the predictions made by the ESA built SCISIM tool, a S/W package which simulates images and spectra by ray-tracing. Globally speaking there is agreement except at energies above 7 keV. Analyses are under way to establish the vignetting function at other off-axis angles and for the other two cameras.

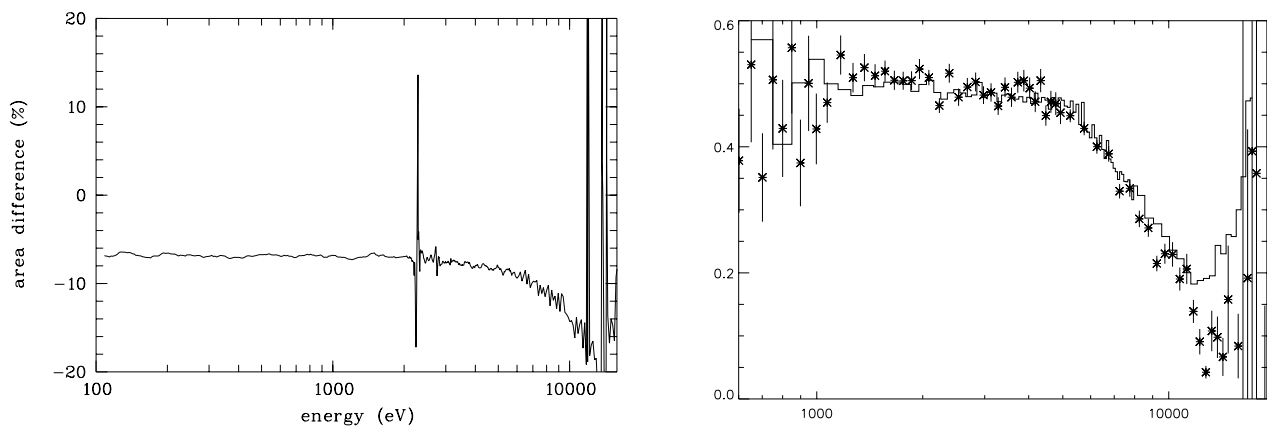


Figure 6. Fig. 6a (*left*): Difference between in-orbit effective area as in current calibration file and perfect mirror module of an XMM-Newton telescope. Difference is attributed to lower reflectance and larger scattering with higher energies, except for the regions close to the M and L absorption edges of gold. Fig. 6b (*right*): Measurement (data) and prediction by ESA's SCISIM tool (histogram) for the vignetting function of an XMM-Newton X-ray telescope at 10 arcmin of-axis; x-axis is in units of eV (graph courtesy D. Lumb).

3. SOME SCIENCE RESULTS

The power of XMM-Newton is to provide spectrally resolved images over a broad energy band of moderate angular and spectral resolution but high dynamical range and high signal-to-noise ratio given the large collecting area of the telescopes and the high quantum efficiency of the CCDs. Furthermore, high signal-to-noise and high resolution spectra are delivered from the RGSs at low energies. The compilation of 56 papers in the January 2001 special issue of *Astronomy & Astrophysics*¹⁶ resulting predominantly from observations made during commissioning, calibration and performance verification demonstrate that these objectives have been met as far as the performance of the instruments is concerned. In the following I add a few more results, some of them being in the process of being submitted to astro-journals.

3.1. The explosion fragments of the Vela supernova remnant

A couple of extended X-ray emission regions outside of the general boundary of the Vela supernova remnant have been discovered²⁸, which were suggested to be composed mainly of stellar fragments of the progenitor star. The spectrum of fragment A measured with ASCA²⁹ indicates a significant overabundance of Si with respect to all other lighter elements which is consistent with the view that this fragment originated deep in the interior of the star, but a quantitative analysis was difficult to do. Figure 7a shows the XMM-Newton EPIC-pn image of fragment A³⁰, of which the head, 10 arcmin x 5 arcmin in size, is the brightest part. Both the tail, which extends back to the SNR boundary, and the head show pronounced structure of surface brightness. Figure 7b is a display of the XMM-Newton EPIC-pn spectrum of the total fragment revealing the presence of strong Mg and Si lines. A preliminary analysis indicates that the Si/O abundance ratio in the head region is about ten times solar, and that of Mg/O about 4 times solar. This results confirms that fragment A is associated with the ejecta. It is noted that there is no indication of S-K H- or He-like lines. The upper limit of the Si/S abundance ratio is just consistent with current core collapse supernova models. The definite determination of this ratio could be a crucial test. Observation times of >100 ks with XMM-Newton would be needed. One of the immediate questions is how such an explosion fragment can survive over a distance of ~20 pc for ~10000 years. Preliminary hydrodynamical models show that this is possible but that the survival time is very sensitive to the ratio of the initial fragment mass to the ambient matter density.

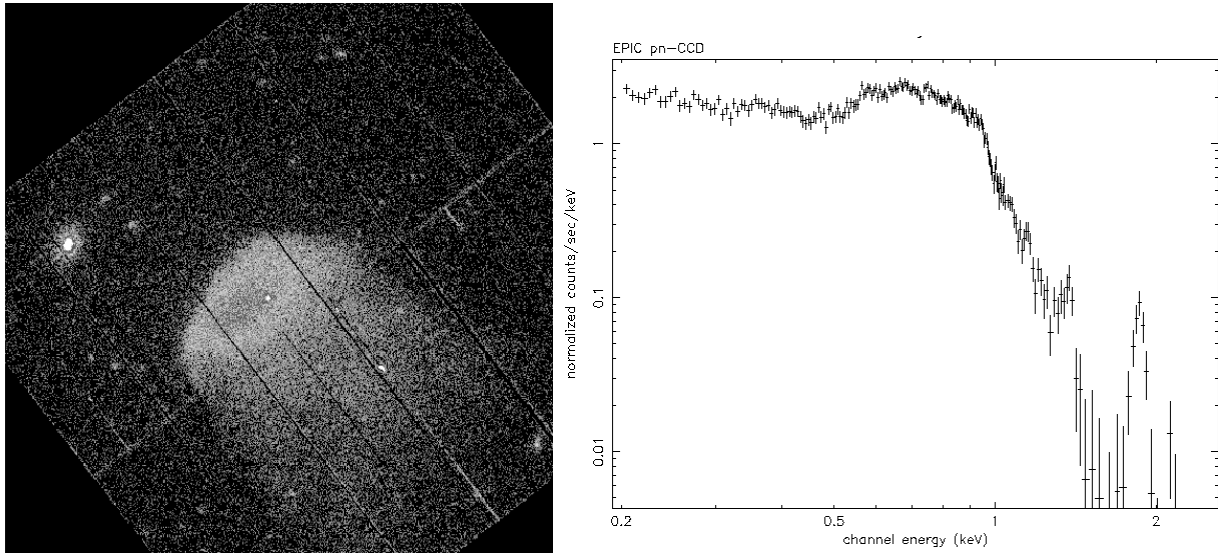


Figure 7. Fig. 7a (*left*): XMM-Newton EPIC-pn raw image of the Vela fragment A and Fig. 7b (*right*) the EPIC-pn spectrum.³⁰

3.2. The Tycho SNR

Unlike the Vela SNR Tycho is just 429 years old and generally considered to be the remnant of a type Ia supernova. Figure 8a shows the XMM-Newton EPIC-MOS broad-band image of the almost circular remnant with an outer annulus of fairly uniform surface brightness and highly knotty structure further inside.

This appearance has brought forward the idea that the outer annulus is associated with the blast wave shock and that the knotty ring contains the reverse shock heated ejecta. Previous X-ray spectra have shown the presence of many H- and He-like K emission lines up to the Fe and Ni K-lines, including a blend of Fe-L lines. With XMM-Newton spatially resolved spectra have been taken³¹, which show a highly non-uniform distribution. The south-eastern rim, which appears to lead the remnant's expansion there, is dominated by three knots. The spectra of each of the knots can be fitted with the same temperature and the same ionization timescale but the abundances of Si, S and Fe differ remarkably. The most northern knot shows the highest abundances of S and Si with some Fe, whereas the most southern knot basically contains no Fe demonstrated by the absence of both the Fe-K and Fe-L lines. In comparison with the other two knots a factor of 10 less Fe seems to have been mixed into the Si layer at the explosion when the knots were formed. The enhancement of Si and S indicates that the matter is from the deeper ejecta and the abundance variations point to a mixing of the deeper Fe layer changing from place to place. In that sense these knots resemble the fragments observed in the Vela SNR, except that the Tycho knots are much younger and may reflect more directly the explosion physics. The angular separation of the knots is $\sim 15^\circ$ and the linear extent of each knot is ~ 0.3 pc, which is remarkably close to the elongation of fragment A of the Vela SNR despite their different ages.

The high energy X-ray continuum is rather regular over the remnant and it peaks just behind the shock front defined by the radio emission, so that it is tempting to attribute the emission to the shocked ambient medium. But the detailed spectral analysis³² shows that this outer region appears to be overabundant in Si and S (c.f. Figure 8b), which is difficult to reconcile with the outer shock. Have we seen the region of the outer shock at all, or is it still fainter than the regions observed so far? Maybe imaging observations at even higher energies may reveal the outer shock region. The XMM-Newton spectra further towards the center of the remnant show the presence of argon and calcium, in particular in the regions where the remnant is brightest (Figure 8b). But the Fe-K line, which requires the highest ionization temperatures, shows up in a region which is just half-way between the center of the remnant and its rim. This is very much in contrast to what is observed in the south-eastern

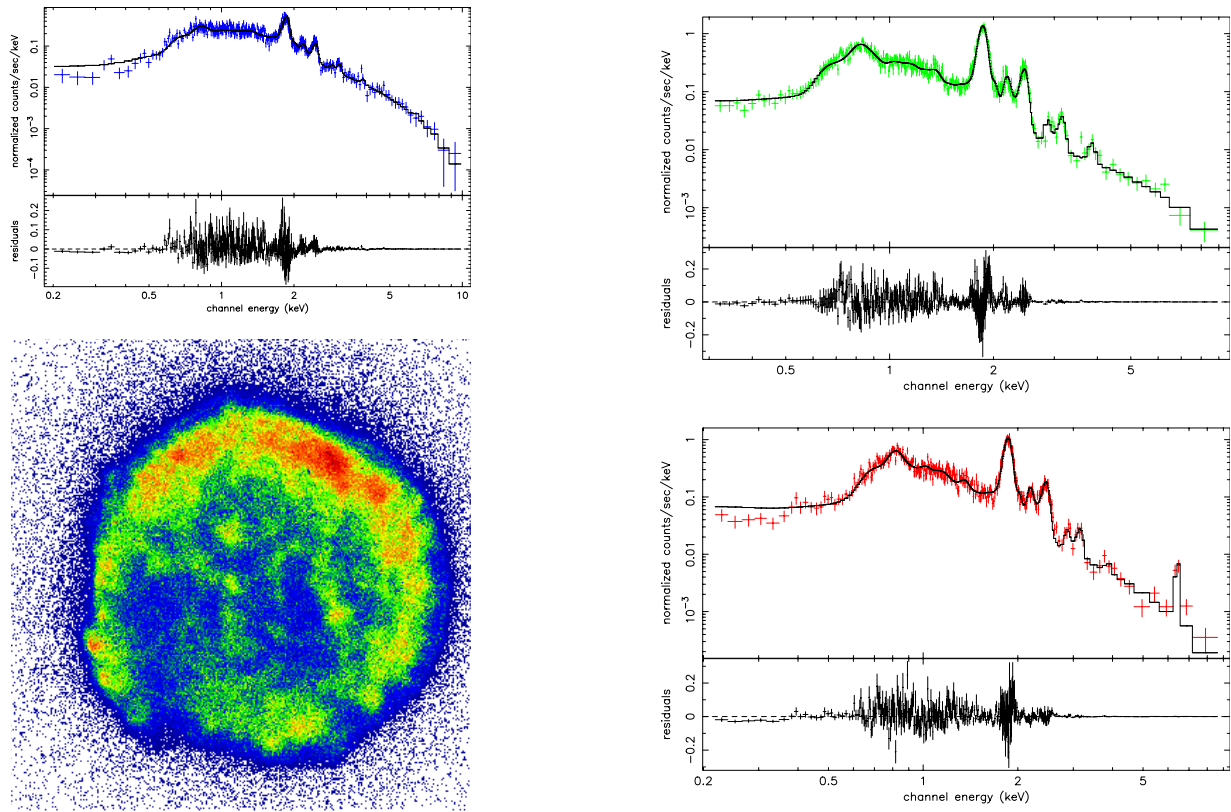


Figure 8. Fig. 8a (*left, bottom*): XMM-Newton EPIC-MOS image of Tycho's supernova remnant³¹; radius of the remnant ~ 240 arcsec. Fig. 8a (*left, top*) & Fig. 8b (*right*): Three EPIC-pn spectra taken from a $\sim 12^\circ$ wide radial cut through the remnant along the south-western direction³²: left top panel spectrum is from the rim (image radius $r > 228$ arcsec); right top panel spectrum is for $190 \text{ arcsec} < r < 220 \text{ arcsec}$; right bottom panel spectrum is for $135 \text{ arcsec} < r < 155 \text{ arcsec}$.

knots where the Fe-K line appears close to the rim in some of them. Consequently, the ionization conditions, the Fe spatial distribution and, most likely, also the Fe velocity distribution are highly asymmetrical throughout Tycho, which probably is related to the explosion details.

3.3. N132D in the Large Magellanic Cloud and the question of the origin of the high energy continuum in SNRs

N132D, a supernova remnant in the LMC, is estimated to be ~ 3000 years old. The remnant, which resembles the Cygnus Loop in its general surface brightness appearance with intriguing filamentary structure and an apparent blow-out to the north-east, has been imaged by Chandra in great detail. Figure 9a shows the first high quality broad-band X-ray spectrum integrated over the remnant obtained with the XMM-Newton EPIC-pn camera³³. Prominent emission lines of Si, S, Ar, Ca and Fe are clearly observed. In itself this spectrum is amazing because it shows the capability of XMM-Newton: the spectrum covers a flux range of 4.5 orders of magnitude in one exposure. Figure 9b shows the high-resolution spectrum obtained with the XMM-Newton RGS spectrometer³⁴, through which 31 emission lines could be identified. For the first time lines from H-like N (#24) and C (#31) are seen and they might provide a link with UV observations. They also allow to better constrain the electron density which is dominated by the elements of low atomic charge. So far, a direct measurement was possible only down to oxygen. Modeling of the RGS spectrum indicates a temperature of ~ 0.6 keV with a definite upper limit of 1 keV. With this temperature and the abundance of Fe apparent in the RGS spectrum in ionic states from

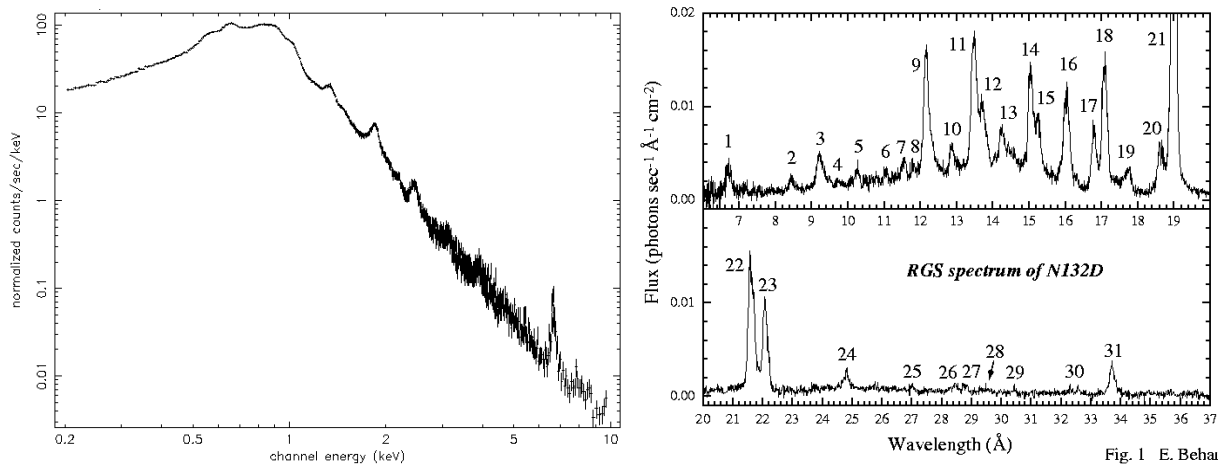


Fig. 1 E. Behar

Figure 9. Fig. 9a (*left*): XMM-Newton EPIC-pn spectrum of the supernova remnant N132D³³; Fig. 9b (*right*) the spectrum resolved with the RGS spectrometer³⁴.

FeXVII to FeXXI essentially no emission of Fe-K is expected, contrary of what the EPIC-pn spectrum shows (c.f. Figure 9a). There must be a high temperature component which produces the high energy continuum and the Fe-K line emission. Interestingly, progressively higher ionic charges of Fe up to FeXXIV are not detected although within the energy range of RGS (strong lines expected at 10.6 and 11.2 Å), which means that plasma of any intermediate temperature between 0.6 keV and a few keV is absent. Furthermore, the spatial distributions of the low temperature and high temperature components are totally different. Whereas the images taken at low ionic charge show pronounced filamentary structure, although different for instance in OVII and OVIII, the high energy continuum and the Fe-K line distributions are fairly uniform across the remnant. There appears to be a high temperature plasma filling the entire volume of the SNR to a large extent whereas the low temperature plasma in the filaments seems to be concentrated on or close to its surface.

The spatial distribution of the high energy continuum is not unique to N132D, a similarly uniform distribution has also been found for Tycho and Cas A. It has been suggested that the high energy continuum is at least partly due to synchrotron radiation from highly relativistic electrons (~ 10 's of TeV) accelerated by diffusive shocks. The first example discussed in this context was SN 1006 and quite a number of SNRs have been added to this category basically because of their power law type X-ray spectra. Diffusive shock acceleration should dominate at the outer shock and the emission should be pronounced there which is not observed for Cas A³⁵. If the high energy continuum is due to synchrotron radiation the acceleration mechanism is more likely to be of turbulent nature acting throughout the remnant.

3.4. SN 1987A

The explosion of SN 1987A was one of the rare historical astronomical events and it has triggered research in many astrophysical fields. In soft X-rays it took a long time, actually almost 3.5 years, to detect emission but since then it has been monitored regularly by ROSAT^{36,38} and more recently by Chandra³⁷ and XMM-Newton³⁸. Figure 10a shows the light curve, which can be remarkably well fitted with a t^2 relation. Soft X-rays are expected from the interaction of the supernova shock with matter left from the wind of the blue supergiant stage of the progenitor inside the inner ring visible in the optical. The t^2 dependence seems to suggest some cylindrical rather than spherical symmetry of the interaction, which would have implications on the matter density of the wind. The XMM-Newton data points tend to exceed the t^2 best fit. Whether this is an indication that the shock wave has already reached and partly penetrated the inner ring around SN 1987A remains to be seen. The Chandra images have resolved the supernova³⁹ indicating that the shock wave has reached the inner surface or is close to contact. In order to convert the count rate of the instruments into flux values the spectrum obtained with the

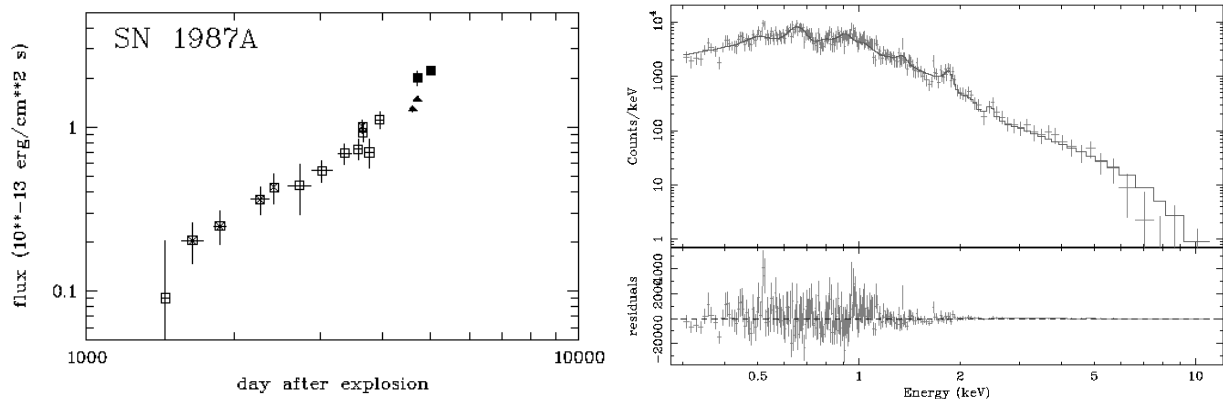


Figure 10. Fig. 10a (*left*): 0.5 – 2.0 keV light curve of SN 1987A compiled from data obtained with ROSAT data (open squares)^{36,38}, Chandra (triangles)³⁷ and XMM-Newton (filled squares)³⁸. Fig. 10b (*right*): Broad band spectrum of SN 1987A obtained with the EPIC-pn camera³⁸.

XMM-Newton EPIC-pn camera (Figure 10b) has been used except for the Chandra data points. The absence of Fe-L and Fe-K emission in the spectrum sets an upper limit of the Fe abundance of 0.03 solar. The abundances of the lighter elements are consistent with 0.5 solar except for Si and S, each of which seems to be overabundant by a few times solar. If confirmed these abundances will play an important role for the understanding of the final evolutionary phase of the SN 1987A progenitor.

Due to the broad band coverage of XMM-Newton a tail in the spectrum has been discovered which adds another component to the spectrum. The tail spectrum is apparently non-thermal and can be best represented by a power law. Right now it is not obvious whether the power law, which has a photon index of -2.6, is the first sign of the putative central pulsar or whether it is associated with the remnant. But the non-thermal flux puts an upper of the pulsar luminosity of $\sim 10^{34}$ erg/s if the circumstellar debris is already optically thin at X-ray energies or $>10^{36}$ erg/s if the intrinsic absorption column density is $>10^{23}$ cm⁻². Alternatively, if the power law spectrum is associated with the remnant we might see the development of X-ray synchrotron radiation at an early phase or the bremsstrahlung of non-thermal electrons. Further monitoring is required and deeper observations should be taken, in particular to look for a different time evolution of the two spectral components.

4. CONCLUSIONS

The XMM-Newton Observatory is performing well. The X-ray telescopes are doing the job they were designed for; in fact the angular resolution is significantly better than originally required. The scientific instruments are delivering a huge amount of new data of outstanding quality and it is without any question that many new discoveries are already on the door step.

REFERENCES

1. "A Cosmic X-ray Spectroscopy Mission", Proc. of a Workshop held in Lyngby, Denmark on 24-26 June 1985, *Proc. ESA SP-239*, 1985.
2. B. Aschenbach, O. Citterio, J.M. Ellwood, P. Jensen, P. de Korte, A. Peacock and R. Willingale, "The High-Throughput X-ray Spectroscopy Mission", Report of the Telescope Working Group, *Proc. ESA SP-1084*, 1987.
3. B. Aschenbach and Heinrich Bräuninger, "Grazing Incidence Telescopes for ESA's X-ray astronomy mission XMM", in *X-ray Instrumentation in Astronomy II*, L. Golub, ed., *Proc. SPIE 982*, pp. 10-15, 1988.

4. B. Aschenbach, "Re-Design of the XMM Optics", *Techn. Note XMM/O/MPE*, 1987.
5. "XMM - Special Issue", ESA Bulletin 100, ESA Publications Division, Noordwijk, The Netherlands, 1999.
6. P. Gondoin, P., B. Aschenbach, M. Beijersbergen, R. Egger, F. Jansen *et al.*, "Calibration of the XMM Flight Mirror Module, I - Image Quality", *Proc. SPIE* **3444**, pp. 278 - 289, 1998.
7. P. Gondoin, P., B. Aschenbach, M. Beijersbergen, R. Egger, F. Jansen *et al.*, "Calibration of the XMM Flight Mirror Module, II - Effective Area", *Proc. SPIE* **3444**, pp. 290 - 301, 1998.
8. L. Strüder, N. Meidinger, E. Pfeffermann, R. Hartmann, H. Bräuninger *et al.*, "X-ray pn-CCDs on the XMM-Newton Observatory", *Proc. SPIE* **4012**, pp. 342 - 352, 2000.
9. L. Strüder, U. Briel, K. Dennerl, R. Hartmann, E. Kendziorra *et al.*, *Astron. & Astroph.* **365**, L18 -L26, 2001.
10. M. J. L. Turner, A. Abbey, M. Arnaud, M. Balasini, M. Barbera *et al.*, "The European Photon Imaging Camera on XMM-Newton: The MOS cameras", *Astron. & Astroph.* **365**, L27 -L35, 2001.
11. J. W. den Herder, A. J. den Boggende, G. Branduardi-Raymont, A. C. Brinkman, J. Cottam *et al.*, "Description and performance of the reflection spectrometer on board of XMM-Newton", *Proc. SPIE* **4012**, pp. 102 - 112, 2000.
12. J. W. den Herder, A. C. Brinkman, S. M. Kahn, G. Branduardi-Raymont, K. Thomson *et al.*, *Astron. & Astroph.* **365**, L7 -L17, 2001.
13. K. O. Mason, A. Breeveld, R. Much, M. Carter, F. A. Cordova *et al.*, "The XMM-Newton optical/UV monitor telescope", *Astron. & Astroph.* **365**, L36 -L44, 2001.
14. U. G. Briel, B. Aschenbach, M. Balasini, H. Bräuninger, W. Burkert *et al.*, "In-Orbit Performance of the EPIC-PN CCD-Camera on Board XMM-Newton", *Proc. SPIE* **4012**, pp. 154 - 164, 2000.
15. K. Dennerl, F. Haberl, B. Aschenbach, U. G. Briel, M. Balasini *et al.*, *Astron. & Astroph.* **365**, L202 -L207, 2001.
16. "First Results from XMM-Newton", *Astron. & Astroph. Letters* **365**, EDP Sciences, Les Ulis, France, 2001.
17. D. de Chambure, R. Lainè, K. van Katwijk, and P. Kletzkine, "XMM's X-Ray Telescopes", in "XMM - Special Issue", ESA Bulletin 100, ESA Publications Division, Noordwijk, The Netherlands, pp. 30 - 42, 1999.
18. B. Aschenbach, "Design of an X-Ray Baffle-System", *Techn. Note XMM-TS-FMP004*, 1996.
19. D. de Chambure, R. Lainè, K. van Katwijk, W. Rühle, D. Schink *et al.*, "The X-ray Baffle of the XMM telescope: Development and Results", Intern. Symposium on the Optical Design and Production, Berlin 1999, *EUROPTO Series 1999*, paper no. 3737-53.
20. E. Pfeffermann, U.G. Briel, H. Hippmann, G. Kettenring, G. Metzner *et al.*, "The focal plane instrumentation of the ROSAT telescope", *Proc. SPIE* **733**, pp. 519-532, 1986.
21. B. Aschenbach, U. Briel, H. Bräuninger, W. Burkert, A. Oppitz *et al.*, "Imaging performance of the XMM-Newton X-ray telescopes", *Proc. SPIE* **4012**, pp. 731 - 739, 2000.
22. M. Güdel, M. Audard, H. Magee, E. Franciosini, N. Grosso *et al.*, "The XMM-Newton view of stellar coronae: Coronal structure in the Castor X-ray triplet", *Astron. & Astroph.* **365**, L344 -L352, 2001.
23. B. L. Henke, E. M Gullikson, J. C. Davis, Atomic Data and Nuclear Data Tables, Vol. 54, July 1993
24. <http://www-cxro.lbl.gov/>

25. A. Owens, S. C. Bayliss, P. J. Durham, S. J. Gurman, and G. W. Fraser, "Apparent discrepancy between measured and tabulated M absorption edge energies", *Astrophys. Journal* **468**, pp. 451 - 454, 1996.
26. R. Willingale, B. Aschenbach, R. G. Griffiths, S. Sembay, R. S. Warwick *et al.*, "New light on the X-ray spectrum of the Crab Nebula", *Astron. & Astroph.* **365**, L212 -L217, 2001.
27. R. S. Warwick, J-P. Bernard, F. Bocchino, A. Decourchelle, P. Ferrando *et al.*, "The extended X-ray halo of the Crab-like SNR G21.5-0.9", *Astron. & Astroph.* **365**, L248 -L253, 2001.
28. B. Aschenbach, R. Egger, and J. Trümper, "Discovery of Explosion Fragments outside the Vela Supernova Remnant Shock-Wave Boundary", *Nature* **373**, pp. 587 - 590, 1995.
29. H. Tsunemi, E. Miyata, and B. Aschenbach, "Spectroscopic Study of the Vela-Shrapnel", *Publ. Astron. Soc. Japan* **51**, pp. 711 - 717, 1999
30. B. Aschenbach and E. Miyata, "XMM-Newton observations of the Vela fragment A", *Astron. & Astrophys.* to be submitted, 2001.
31. A. Decourchelle, J. L. Sauvageot, M. Audard, B. Aschenbach, S. Sembay *et al.*, "XMM-Newton observations of the Tycho supernova remnant", *Astron. & Astroph.* **365**, L218 -L224, 2001.
32. T. F. X. Stadhauer and B. Aschenbach, "Spatially resolved spectroscopy of Tycho's SNR", Proc. X-ray Symp. "New Century of X-ray Astronomy", Yokohama, Japan, March 2001, to be publ. in *Astron. Soc. Pac.*, 2001.
33. K. Dennerl and A. Read, priv. communication, 2000.
34. E. Behar, A. P. Rasmussen, R. G. Griffiths, K. Dennerl, M. Audard *et al.*, "High resolution X-ray spectroscopy and imaging of the supernova remnant N132D", *Astron. & Astroph.* **365**, L242 -L247, 2001.
35. J. A. M. Bleeker, R. Willingale, K. van der Heyden, K. Dennerl, J. S. Kaastra *et al.*, "Cassiopeia A: On the origin of the hard X-ray continuum and the implication of the observed OVIII Ly- α /Ly- β distribution", *Astron. & Astroph.* **365**, L225 -L230, 2001.
36. G. Hasinger, B. Aschenbach, and J. Trümper, "The X-ray lightcurve of SN 1987 A", *Astron. & Astroph.* **312**, L9 -L12, 1996.
37. D. N. Burrows, E. Michael, U. Hwang, R. McCray, R. A. Chevalier *et al.*, "The X-ray remnant of SN 1987A", *Astrophys. Journal* **543**, L149 - L152, 2000.
38. B. Aschenbach, "Supernova remnants - the past, the present and the future", Proc. X-ray Symp. "New Century of X-ray Astronomy", Yokohama, Japan, March 2001, to be publ. in *Astron. Soc. Pac.*, 2001.
39. D. N. Burrows, E. Michael, U. Hwang, R. Chevalier, G. P. Garmire *et al.*, "Early Results from Chandra Observations of Supernova Remnants", *Proc. SPIE* **4012**, pp. 91 - 100, 2000.